JNeurosci
THE JOURNAL OF NEUROSCIENCE

Research Articles: Behavioral/Cognitive

Overlooked tertiary sulci serve as a meso-scale link between microstructural and functional properties of human lateral prefrontal cortex

https://doi.org/10.1523/JNEUROSCI.2362-20.2021

Cite as: J. Neurosci 2021; 10.1523/JNEUROSCI.2362-20.2021

Received: 8 September 2020
Revised: 22 December 2020
Accepted: 5 January 2021

Title: Overlooked tertiary sulci serve as a meso-scale link between microstructural and functional properties of human lateral prefrontal cortex

Abbreviated title: Tertiary sulcal morphology in human prefrontal cortex

Jacob A. Miller[1*], Willa I. Voorhies[1,2], Daniel J. Lurie[2], Mark D'Esposito[1,2], Kevin S. Weiner[1,2]

[1]Helen Wills Neuroscience Institute, [2]Department of Psychology,
University of California-Berkeley

***Corresponding author:**
Jacob A. Miller
jacob_miller@berkeley.edu
210 Barker Hall
University of California-Berkeley
Berkeley, CA, 94720

Figures
Figures: 9
Tables: 2
Extended Data Figures: 2

Word counts
Abstract: 250
Introduction: 638
Discussion: 1313
Significance Statement: 118

Keywords: prefrontal cortex, functional neuroanatomy, morphology, gradients, connectivity, brain mapping

Abstract

Understanding the relationship between neuroanatomy and function in portions of cortex that perform functions largely specific to humans such as lateral prefrontal cortex (LPFC) is of major interest in systems and cognitive neuroscience. When considering neuroanatomical-functional relationships in LPFC, shallow indentations in cortex known as tertiary sulci have been largely unexplored. Here, by implementing a multi-modal approach and manually defining 936 neuroanatomical structures in 72 hemispheres (in both males and females), we show that a subset of these overlooked tertiary sulci serve as a meso-scale link between microstructural (myelin content) and functional (network connectivity) properties of human LPFC in individual participants. For example, the *posterior middle frontal sulcus* (*pmfs*) is a tertiary sulcus with three components that differ in their myelin content, resting state connectivity profiles, and engagement across meta-analyses of 83 cognitive tasks. Further, generating microstructural profiles of myelin content across cortical depths for each *pmfs* component and the surrounding middle frontal gyrus (MFG) shows that both gyral and sulcal components of the MFG have greater myelin content in deeper compared to superficial layers and that the myelin content in superficial layers of the gyral components is greater than sulcal components. These findings support a classic, yet largely unconsidered theory that tertiary sulci may serve as landmarks in association cortices, as well as a modern cognitive neuroscience theory proposing a functional hierarchy in LPFC. As there is a growing need for computational tools that automatically define tertiary sulci throughout cortex, we share *pmfs* probabilistic sulcal maps with the field.

Significance statement

Lateral prefrontal cortex (LPFC) is critical for functions that are thought to be specific to humans compared to other mammals. However, relationships between fine-scale neuroanatomical structures largely specific to hominoid cortex and functional properties of LPFC remain elusive. Here, we show that these structures, which have been largely unexplored throughout history, surprisingly serve as markers for anatomical and functional organization in human LPFC. These findings have theoretical, methodological, developmental, and evolutionary implications for improved understanding of neuroanatomical-functional relationships not only in LPFC, but also in association cortices more broadly. Finally, these findings ignite new questions regarding how morphological features of these neglected neuroanatomical structures contribute to functions of association cortices that are critical for human-specific aspects of cognition.

Introduction

Understanding how anatomical structures of the brain support functional gradients and networks that perform computations for human-specific aspects of cognition is a major goal in systems and cognitive neuroscience. Of the many anatomical structures to target, lateral prefrontal cortex (LPFC) is expanded in the human brain relative to non-human primate species commonly used in neuroscience research, such as rhesus macaques (Semendeferi et al., 2002; Donahue et al., 2018; Barrett et al., 2020), and is particularly important given its central role in cognitive control and goal-directed behavior (Miller and Cohen, 2001; Szczepanski and Knight, 2014). Major progress has been made in understanding the relationship between the functional organization and the large-scale cortical anatomy of human LPFC. For example**,** previous findings support a hierarchical functional gradient organized along the rostral-caudal anatomical dimension of LPFC spanning several centimeters (Badre and D'Esposito, 2009; Nee and D'Esposito, 2016; Demirtas et al., 2019). Beyond this large-scale organization of human LPFC, it is largely unknown if more fine-grained structural-functional relationships exist. Thus, to begin to fill this gap in knowledge, we sought to answer the following question in the present study: Do individual differences in fine-grained morphological features of LPFC shed light on microstructural and functional properties of LPFC?

An important morphological feature of cortex is the patterning of the indentations, or sulci. Indeed, 60-70% of the cortex is buried in sulci and some sulci serve as landmarks that identify different cortical areas, especially in primary sensory cortices (Van Essen and Dierker, 2007; Zilles et al., 2013). In these cases, merely identifying a sulcus provides functional insight (Hinds et al., 2008). Despite this widely replicated relationship between sulcal morphology and functional representations in primary sensory cortices, much less is known regarding the

predictability between shallow, tertiary sulci and functional representations in association cortex, especially LPFC. A classic theory proposed by Sanides (1964) hypothesized that the late emergence and protracted development of tertiary sulci may co-occur with microstructural and functional features of association cortices, along with cognitive functions such as sustained attention and "active thinking" (Sanides, 1964) that also develop fully after adolescence (Fisher, 2019).

However, at least two factors have prevented the examination of tertiary sulci relative to anatomical and functional organization in human LPFC. First, tertiary sulci are presently excluded from nearly all published neuroanatomical atlases because classic anatomists could not discriminate tertiary sulci from indentations produced by veins and arteries on the outer surface of the cerebrum in post-mortem tissue, which is considered the gold standard of anatomical research (Weiner et al., 2018). Consequently, tertiary sulci within the posterior middle frontal gyrus (MFG) were either undefined in classic atlases or conflated with more anterior structures (**Figure 1**; (Miller et al., 2020a)). Second, the majority of human functional magnetic resonance imaging (MRI) studies of LPFC implement group analyses on average brain templates. As shown in **Figure 1**, averaging cortical surfaces together causes tertiary sulci in LPFC to disappear, especially within the posterior MFG.

[INSERT FIGURE 1 HERE]

Here, we implemented a multi-modal approach demonstrating that identifying individual sulci in LPFC reveals that the *posterior middle frontal sulcus* (*pmfs*) serves as a meso-scale link between microstructural (myelin content) and functional (network connectivity) properties of human LPFC in individual participants. Specifically, after manually labeling LPFC tertiary sulci

in 72 hemispheres based on a recently proposed labeling scheme (Petrides and Pandya, 2012; Petrides, 2019), we found that three components of the *pmfs* are dissociable based on myelin content, resting state functional connectivity profiles, and cognitive task activations. Moreover, the *pmfs* shows a distinct microstructural profile of myelin content across cortical depths from the surrounding MFG and distinct functional activations from the *intermediate frontal sulcus* (*imfs*). Together, these results not only provide important evidence that individual differences in LPFC sulcal patterning reflect meaningful differences in microstructural and functional properties, but also suggest that the *pmfs* serves as a bridge to Sanides' classic hypothesis.

Materials and Methods

In the sections below, we describe the data used and the analysis methods implemented in three separate sections: 1) the general approach and a description of the multi-modal datasets that were used, 2) a detailed description of the methodology used for sulcal labeling within individual participants, and 3) the calculation of anatomical and functional metrics.

General approach

We sought to characterize sulcal morphology at the individual level in the LPFC of the human brain. To implement this process, we manually defined sulci following the most recent and comprehensive proposed labeling of sulci in the frontal lobe (Petrides and Pandya, 2012; Petrides, 2019). As in our prior work (Weiner et al., 2014; Weiner et al., 2018), all sulci were defined in native space cortical surfaces and individual hemispheres, which enables the most accurate definition of tertiary sulci within *in vivo* MRI data.

Multi-modal HCP dataset

We analyzed a subset of the multi-modal MRI data available for individual participants from the Human Connectome Project (HCP). We began with the first 5 numerically listed HCP participants and then randomly selected 31 additional human participants from the HCP for a total of 36 individuals (17 female, 19 male, age range 22-36 years).

Anatomical T_1-weighted (T_1w) MRI scans (0.7 mm voxel resolution) were obtained in native space from the HCP database, along with outputs from the FreeSurfer pipeline slightly modified by the HCP (Dale et al., 1999; Fischl et al., 1999a; Glasser et al., 2013). Maps of the ratio of T_1-weighted and T_2-weighted scans, which is a measure of tissue contrast enhancement related to

myelin content, were downloaded as part of the HCP 'Structural Extended' release. All additional anatomical metrics, which are detailed in the next section, were calculated on the full-resolution, native FreeSurfer (https://surfer.nmr.mgh.harvard.edu/) meshes (Dale et al., 1999; Fischl et al., 1999a; Fischl et al., 1999b).

Anatomical labeling and metrics

Manual sulcal labeling

Guided by a recent comprehensive proposal for labeling sulci in LPFC (Petrides, 2019), each sulcus was manually defined within each individual hemisphere on the FreeSurfer *inflated* mesh with *tksurfer*. The *curvature* metric in FreeSurfer distinguished the boundaries between sulcal and gyral components, and manual lines were drawn to separate sulcal components based upon the proposal by Petrides and colleagues (Amiez and Petrides, 2007; Petrides and Pandya, 2012; Petrides, 2019; Germann and Petrides, 2020), as well as the appearance of sulci across the *inflated*, *pial*, and *smoothwm* surfaces. We maintained the number of components for all tertiary sulci (e.g., the three components of the *posterior* m*iddle frontal sulcus* - *pmfs*) based on the proposal by Petrides and colleagues to test if each of these sulcal components could be defined in a relatively large sample size (N=72) of *in vivo* hemispheres. The labels were generated using a two-tiered procedure. The labels were first defined manually by J.M. and W.V. and then finalized by a neuroanatomist (K.S.W.). All anatomical labels for a given hemisphere were fully defined before any morphological or functional analysis of the sulcal labels was performed. The superior, inferior, posterior, and anterior boundaries of our cortical expanse of interest were the following sulci, respectively: (1) the anterior and posterior components of the *superior frontal sulcus*, (2) the *inferior frontal sulcus*, (3) the *central sulcus*, and (4) the horizontal (*imfs-h*) and

vertical (*imfs-v*) intermediate frontal sulci. In each hemisphere, we first labeled the large primary sulci such as the central sulcus before labeling the secondary (e.g. *sfs*, *ifs*, *imfs*) sulci, and then we identified the tertiary sulcal components of the *pmfs*. Primary, secondary, and tertiary labels refer to the time in which the sulci emerge in gestation (Sanides, 1964; Chi et al., 1977; Welker, 1990; Armstrong et al., 1995). An example hemisphere with every sulcus labeled within these boundaries is shown in **Figure 2a**, and the *pmfs* sulcal components are plotted on each hemisphere in **Extended Data Figure 2-1**.

Quantification of sulcal depth and surface area

Sulcal depth was calculated from the native meshes generated by the FreeSurfer HCP pipeline. Raw values for sulcal depth (mm) were calculated from the sulcal fundus to the smoothed outer pial surface using a custom-modified version of a recently developed algorithm for robust morphological statistics building on the FreeSurfer pipeline (Madan, 2019). Surface area (mm^2) was generated for each sulcus through the *mris_anatomical_stats* function in FreeSurfer (Dale et al., 1999; Fischl et al., 1999a). We focused on sulcal depth as it is the main measurement that is used to discriminate tertiary sulci from primary and secondary sulci. Specifically, primary sulci are deepest, while tertiary sulci are shallowest, and secondary sulci are in between (Sanides, 1964; Chi et al., 1977; Welker, 1990; Armstrong et al., 1995). We also included surface area as tertiary sulci typically also have a reduced surface area compared to primary and secondary sulci.

Calculating T_1w/T_2w myelin index along an anterior-posterior dimension in LPFC

In order to test if there is a relationship between any of our sulci of interest and myelin content, we used an *in vivo* proxy of myelination: the T_1w/T_2w maps for each individual hemisphere

(Glasser and Van Essen, 2011; Shams et al., 2019). To generate the T_1w/T_2w maps, two T1- and T2-weighted images from each participant were registered together and averaged as part of the HCP processing pipeline (Glasser et al., 2013). The averaging helps to reduce motion-related effects or blurring. Additionally (and as described in Glasser et al., 2013), the T_1w/T_2w images were bias-corrected for distortion effects with field maps. We averaged the T_1w/T_2w value across each vertex for each sulcus in order to test if the *pmfs* sulcal components are separable based on myelin content (**Figure 3**). We further sought to characterize the relationship between morphology and myelin by determining if there was an anterior-posterior gradient of myelination across individual hemispheres. To do so, we first calculated the minimum geodesic distance of each vertex from the central sulcus. Geodesic distance was calculated on the *fiducial* surface using algorithms in the pycortex package (Gao et al., 2015). Then, we averaged across the vertices within each sulcus and tested for a linear relationship between average distance from the central sulcus and myelin content. To take advantage of each participant's individual data, we built a mixed linear model (random intercepts) in the *lme4* R package, using sulci and hemisphere as explanatory variables to correlate with average myelin content (**Figure 3**).

Sampling T_1w/T_2w myelin index across cortical depths

In order to investigate the microstructural profile of the *pmfs* across cortical layers, we generated nine surfaces from the outermost (*pial*) to the innermost (*white matter)* layers in all of the manually labeled hemispheres using an equivolumetric approach (Waehnert et al., 2014). We implemented the equivolume surface algorithm spanning nine cortical depths with the *surfacetools* Python package that builds on top of FreeSurfer (Dale et al., 1999) outputs: https://github.com/kwagstyl/surface_tools. The high-resolution T_1w/T_2w volumetric data in each

HCP participant's native anatomical space were then sampled onto each equivolume surface using the FreeSurfer *mri_vol2surf* function to obtain a value of T_1w/T_2w at each cortical depth. The stability of depth profiles of T_1w/T_2w values extracted from individual regions was shown to be highest in the same HCP dataset when using a solution of 14 equivolume surfaces, with stability plateauing when using nine or more equivolume surfaces (Paquola et al., 2019). We compared the mean T_1w/T_2w value across depths for each participant in the manually defined *pmfs* components and the surrounding middle frontal gyrus (as defined by FreeSurfer parcellations (Destrieux et al., 2010), but with the *pmfs* components removed). We then conducted a repeated-measures ANOVA followed by post-hoc *t*-tests at each depth to test for differences in myelin content between the *pmfs* components and the *MFG* (**Figure 5**). Tests across each of the nine cortical depths were corrected for multiple comparisons at a familywise error (FWE) threshold of $p = 0.05/9$.

Cross-validation of sulcal location

In order to quantify the ability to predict the location of each sulcus across participants, we registered all sulcal labels to a common template surface (*fsaverage*) using cortex-based alignment (Fischl et al., 1999b). Similarity between each transformed individual label and the labels defined on *fsaverage* was calculated via the DICE coefficient, where X and Y are each label:

$$DICE(X,Y) = \frac{2|X \cap Y|}{|X| + |Y|}$$

The cortex-based alignment algorithm aligns the surfaces based on sulcal depth and curvature metrics. We use the central sulcus as a proxy noise ceiling measurement for DICE coefficient

values from other frontal sulci because it is a large and deep sulcus and is used in the surface registration algorithm that aligns cortical surfaces across participants (Fischl et al., 1999b).

Sulcal probability maps were calculated to describe the vertices with the highest alignment across participants for a given sulcus. A map was generated for each sulcus by calculating, at each vertex in the *fsaverage* hemisphere, the number of participants with that vertex labeled as the given sulcus, divided by the total number of participants. In order to avoid overlap among sulci, we then constrained the probability maps into *maximum probability maps* (MPMs) by only including vertices where (1) greater than 33% of participants included the given sulcal label and (2) the sulcus with the highest value of participant overlap was assigned to a given vertex. In a leave-one-participant out cross-validation procedure, we generated probability maps from n = 35 participants and registered the probability map to the held-out participant's native cortical surface. This provided a measure of sulcal variability and prediction accuracy (**Figure 8**). This procedure also allows the identification of the *pmfs* sulcal components within held-out individual participants, reducing the extent of manual labeling necessary to identify this structure in future studies. Finally, the MPMs were used when analyzing meta-analytical functional data (described in the section *Cognitive Component Modeling*) and whole brain population receptive field data (**Figure 7**). The MPMs and code for alignment to new participants will be available on OSF with the publication of this paper.

Functional metrics

Resting-state network connectivity fingerprints

In order to test if the three *pmfs* sulcal components were functionally distinct from one another, we calculated and compared functional connectivity network fingerprints for each sulcus.

Resting-state network parcellations for each individual participant were used from Kong et al. (2018), who generated individual network definitions by applying a hierarchical Bayesian network algorithm to produce maps for each of 17-networks (Yeo et al., 2011) in individual HCP participants. These data were calculated in the template HCP *fs_LR 32k* space. We resampled the network profiles for each participant onto the *fsaverage* cortical surface and, then, to each native surface using CBIG tools (https://github.com/ThomasYeoLab/CBIG). We then calculated the overlap of each *pmfs* sulcus in each participant with each of the 17 resting-state networks. We also separated the components of the *pmfs* and tested whether they showed similar or different network connectivity fingerprints using a 3-way repeated-measures ANOVA (sulcal component x network x hemisphere). Variability across individuals in the network profiles for each *pmfs* component was calculated by generating the Wasserstein metric (Earth Mover's Distance) between the resting-state network overlap values for each unique pair of participants (**Figure 5b**).

Cognitive component modeling

To further examine if the *pmfs-p, pmfs-i, and pmfs-a* are functionally distinct, we quantified the overlap between the *maximum probability maps* (MPMs) of each sulcal component and meta-analytic fMRI data from hundreds of experiments aligned to the *fsaverage* surface. Specifically, we quantitatively related the sulcal MPMs to vertex-wise maps for 14 cognitive components, which quantify how each vertex is recruited in a given set of cognitive operations across tasks and experiments (Yeo et al., 2015). We used a Bayesian method of expectation maximization to determine the combination of cognitive components that best fit each sulcal MPM. This resulted in a set of probabilities for each cognitive component for each sulcal map. We tested whether all

sulci and the three components of the *pmfs* were distinguishable based upon these cognitive component loadings from a repeated-measures ANOVA (**Figure 6**).

Retinotopic response mapping

To determine if there was any correspondence between the manually labeled LPFC sulci and retinotopic representations, we analyzed a recent population receptive field mapping dataset (Benson et al., 2018). As these data were only available in a template (*fsaverage*) space, we used the predicted sulcal locations from probabilistic maps (as used in the cognitive components analysis) for these analyses (**Figure 7**). For each sulcus, we extracted the mean R^2 value (the percentage of variance in each vertex explained by the population receptive field model) across participants for vertices that showed meaningful retinotopic responses (thresholded at $R^2 > 10\%$, as in (Mackey et al., 2017)).

Statistical methods

All repeated measures ANOVAs (including sphericity correction) and post-hoc t-tests were performed with the *afex* and *emmeans* R packages, imported into Python via *rpy2*. For each repeated measures ANOVA, cortical hemisphere and sulcus were used as within-subject factors. Effect sizes for each main effect and interaction were calculated and reported with the *generalized eta-squared* metric (Fritz et al., 2012). Mixed linear models were implemented in the *lme4* R package. Cortical surface files were loaded in and operated on in Python using the nilearn software: https://nilearn.github.io

Results

Before conducting our multimodal examination relating morphological features of tertiary sulci to microstructural and functional properties of LPFC, we first had to confront the contradictory nature of historic and modern definitions of sulci within the middle frontal gyrus (MFG). For example, sulcal definitions within the MFG vary in a) their nomenclature, b) the number of sulcal components depicted or acknowledged in schematics, c) the omission or inclusion of sulci within the posterior MFG, and d) the actual empirical data that is included to support the illustration of the sulcal patterning (**Figure 1**). To ameliorate these concerns and to either empirically support or to refute the generality of sulcal definitions within the posterior MFG, we apply a classic, multimodal approach that has been used to distinguish cortical areas from one another in order to determine sulcal definitions in the posterior MFG. Specifically, after identifying each sulcus within the posterior MFG based on recent proposals (Petrides and Pandya, 2012; Petrides, 2019), we use both anatomical and fMRI data to either support or refute the identification of individual sulci within this cortical expanse. Implementing this two-pronged approach, we first examined if the three components of the posterior middle frontal sulcus (*pmfs*) are consistently identifiable within individual hemispheres. And if so, we then tested if the three *pmfs* components are anatomically and functionally homogenous, or serve to identify anatomical and functional heterogeneity in LPFC. This approach supports the latter in which there are three anatomically and functionally distinct sulci within the posterior MFG: the posterior (*pmfs-p*), intermediate (*pmfs-i*), and anterior (*pmfs-a*) posterior middle frontal sulci.

[INSERT FIGURE 2 HERE]

Three posterior middle frontal sulci (pmfs) are identifiable within individuals and are characteristically shallow

Before examining the sulcal patterning within the posterior MFG, we first identified reliable sulci (**Materials and Methods**: *manual sulcal labeling*) surrounding the MFG in both *in vivo* cortical surface reconstructions of MRI data and post-mortem brains (**Figure 2a**). Posteriorly, we identified the central sulcus (*cs*), as well as the superior (*sprs*) and inferior (*iprs*) pre-central sulci. Superiorly, we identified the anterior (*sfs-a*) and posterior (*sfs-p*) superior frontal sulci. Inferiorly, we identified the inferior frontal sulcus (*ifs*). Anteriorly, we identified the horizontal (*imfs-h*) and vertical (*imfs-v*) intermediate frontal sulci. The latter two sulci are consistent with Eberstaller's classic definition of the middle frontal sulcus, but have since been renamed (**Figure 1**; (Miller et al., 2020a)). Within the posterior MFG, we identified three sulci in every hemisphere (N=72). From posterior to anterior, the first sulcus (*pmfs-p*) is positioned immediately anterior to the *sprs* (**Figure 2a**, **Extended Data Figure 2-1**), and most commonly does not intersect other sulci (see **Table 1** for a summary of the morphological patterns, or types). The second sulcus (*pmfs-i*) is located immediately anterior to the *pmfs-p*, and typically aligns with the separation between the *sfs-a* and *sfs-p* components. The *pmfs-i* is most often independent (especially in the right hemisphere) or intersects (especially in the left hemisphere) the *pmfs-a*. Finally, the third sulcus (*pmfs-a*) is immediately anterior to the *pmfs-i*, inferior to the *sfs-a*, and posterior to the *imfs-h*. The *pmfs-a* most commonly intersects other sulci in the right hemisphere.

[INSERT TABLE 1 HERE]

Each sulcus is also identifiable within individual *in vivo* volumetric slices (Petrides, 2019) and in postmortem brains (**Figure 2**), which indicates that the computational process used to generate the cortical surface reconstruction in the MRI data does not artificially create these sulci within the MFG. Our results show that the *pmfs* is distinguishable from the *imfs*, which is in correspondence with the recent atlas from Petrides (2019), whereas the *pmfs* and *imfs* were often combined in classic sulcal atlases (Ono et al., 1990).

The two most identifying morphological features of the three *pmfs* sulci are their surface area and depth (**Figure 2b**). Each *pmfs* sulcus is of roughly equal surface area (**Figure 2b**, **Table 2**), which is smaller than the surface area of the other examined sulci in LPFC (**Figure 2b**, **Table 2**). A two-way repeated-measures ANOVA with factors sulcus and hemisphere yielded a main effect of sulcus ($F(5.78, 202.15) = 384.1$, $p < 0.001$, $\eta_G^2 = 0.84$) and no main effect of hemisphere ($F(1, 35) = 0.1$, $p = 0.77$). The depth of the three *pmfs* sulci are also the shallowest of the lateral PFC sulci examined (**Figure 2b, Table 1**). A two-way repeated-measures ANOVA with sulcus and hemisphere as factors yielded a main effect of sulcus ($F(3.15, 103.84) = 77.7$, $p < 0.001$, $\eta_G^2 = 0.55$), and a main effect of hemisphere ($F(1, 33) = 20.4$, $p < 0.001$, $\eta_G^2 = 0.02$) in which sulci were deeper in the right compared to the left hemisphere (**Figure 2b**, **Table 2**). Post-hoc tests show that, across hemispheres, the *pmfs-p* is shallower than all other sulci (p-values < 0.001, Tukey's adjustment), and the *pmfs-i* and *pmfs-a* are shallower than all other sulci except for the *imfs-v*. Taken together, three *pmfs* sulci are identifiable in individual hemispheres (**Figure 2**, **Extended Data Figure 2-1**) and distinguish themselves from other LPFC sulci based on their surface area and shallowness.

[INSERT TABLE 2 HERE]

The pmfs-p, pmfs-i, and pmfs-a are anatomically dissociable and reflect a larger rostro-caudal myelination gradient in LPFC

While the *pmfs-p*, *pmfs-i*, and *pmfs-a* are morphologically distinct from surrounding sulci (**Figure 2**), it is presently unknown if they are anatomically and functionally similar or distinct from one another. To test this, we first extracted and compared average MRI T_1w/T_2w ratio values from each sulcus. The T_1w/T_2w ratio is a tissue contrast enhancement index that is correlated with myelin content (**Figure 3a**; (Glasser and Van Essen, 2011; Shams et al., 2019)). We chose this index because myeloarchitecture is a classic criterion used to separate cortical areas from one another (Vogt and Vogt, 1919; Flechsig, 1920; Hopf, 1956; Dick et al., 2012). A two-way repeated-measures ANOVA with sulcus and hemisphere as factors yielded a main effect of sulcus ($F(1.76, 61.7) = 85.0$, $p < 0.001$, $\eta_G^2 = 0.39$) and a main effect of hemisphere ($F(1, 35) = 10.5$, $p = 0.003$, $\eta_G^2 = 0.05$) on myelin content, but no sulcus x hemisphere interaction ($F(1.73, 60.5) = 2.5$, $p = 0.10$). The differences in myelin across sulci were driven by the finding that T_1w/T_2w decreased from posterior to anterior across hemispheres: *pmfs-p* vs. *pmfs-i*, $t(70) = 9.75$, $p < 0.001$ (Tukey's post-hoc), *pmfs-i* vs. *pmfs-a*, $t(70) = 2.62$, $p = 0.029$, and *pmfs-p* vs. *pmfs-a*, $t(70) = 12.37$, $p < 0.001$. The right hemisphere also had higher myelin content overall in the *pmfs*, $t(35) = 3.25$, $p = 0.003$. Accordingly, the three sulcal components are differentiable based on myelin content in both hemispheres (**Figure 3b**).

[INSERT FIGURE 3 HERE]

The rostro-caudal gradient among the *pmfs-p*, *pmfs-i*, and *pmfs-a* sulci is embedded within a larger rostro-caudal myelination gradient in lateral PFC. Specifically, modeling T_1w/T_2w content across frontal sulci as a function of distance from the central sulcus (**Figure 3c**)

using a mixed linear model revealed a significant, negative effect of distance from the central sulcus along the rostral-caudal axis (β= -0.001, z = -33.8, p < 0.001), with no differences between hemispheres (β= -0.003, z = -0.8, p = 0.4). Together, our quantifications show that the *pmfs-p*, *pmfs-i*, and *pmfs-a* are embedded within a larger anatomical and functional hierarchical gradient in LPFC (see **Discussion** for further details).

The pmfs components show a microstructural profile across cortical layers that is distinct from the middle frontal gyrus (MFG)

Classic and modern findings show that there is generally more intracortical myelin in deeper cortical layers and that the depths of sulci often have less myelinated fibers than gyral crowns (Braitenberg, 1962; Sanides, 1972; Welker, 1990; Annese et al., 2004; Rowley et al., 2015). Building on this work, we sought to calculate microstructural profiles for myelin content across cortical depths for each *pmfs* component, as well as the gyral components of the MFG that surround them (**Figure 4**; **Materials and Methods**). To do so, we implemented equivolume algorithms to construct cortical surfaces within the gray matter. The depth profiles from equivolume surfaces have been used to investigate cortical laminar organization *in vivo* and correspond with those obtained from both *ex vivo* MRI data and post-mortem histological sections (Waehnert et al., 2014; Paquola et al., 2019).

[INSERT FIGURE 4 HERE]

The MFG and *pmfs* components show distinct microstructural profiles of myelin content across cortical depths. A three-way repeated-measures ANOVA with factors of structure (*pmfs-p, pmfs-i, pmfs-a, MFG*), cortical depth (*0%, 12.5%, 25%, 37.5%, 50%, 62.5%, 75%, 87.5%, 100%*), and hemisphere (*left, right*), yields main effects of structure ($F(2.26, 78.94) = 15.6$, $p < 0.001$, $\eta_G^2 = 0.007$), depth ($F(1.39, 48.49) = 1849.6$, $p < 0.001$, $\eta_G^2 = 0.84$), and a structure x depth interaction ($F(6.78, 237.43) = 78.5$, $p < 0.001$, $\eta_G^2 = 0.02$). This interaction between structure and depth did not differ by hemisphere ($F(4.69, 164.26) = 1.13$, $p = 0.35$, $\eta_G^2 = 0.02$), so subsequent analyses are collapsed across hemispheres. To determine which differences drive the distinct profiles in myelin content across cortical layers between the *pmfs* and MFG, we conducted post-hoc tests at each cortical depth (**Figure 4a**). The MFG had higher myelin content in each of the upper cortical depths (0%, 12.5%, 25%, 37.5%)

compared to all of the *pmfs* components (all *p-values* < 0.001, FWE-corrected at α = 0.05/9 for the 9 cortical depths). In the middle-to-deep layers (50%, 62.5%), the *pmfs-p* had higher myelin content than either the *pmfs-i* (50%: t(105) = 6.4, p < 0.001; 62.5%: t(105) = 7.0, p < 0.001) or *pmfs-a* (50%: t(105) = 7.1, p < 0.001; 62.5%: t(105) = 8.1, p < 0.001), and was even higher than the MFG (50%: t(105) = 0.27, p = 0.99; 62.5%: t(105) = 3.7, p = 0.002). At the deepest cortical layers, closest to the gray/white matter boundary, all three *pmfs* components showed increased myelin relative to the MFG. Specifically, the *pmfs-a* showed the highest myelin content in the deepest layers, but all three *pmfs* components displayed higher myelin than the MFG (all *p-values* < 0.001, FWE-corrected at α = 0.05/9 for the 9 cortical depths). The profile of myelin content across cortical depths in the *pmfs* and MFG is also robust when comparing myelin content at a coarser (3 instead of 9) level of upper, middle, and lower depths (mean of depths within each bin): structure x depth interaction ($F(3.87, 135.4) = 127.4$, p < 0.001, $\eta_G^2 = 0.02$). Altogether, the *pmfs* differed from the MFG in microstructure across cortical layers, with lower myelin content in upper layers and higher myelin content in deeper layers. This surface-based sampling of cortical depths provides *in vivo* neuroimaging evidence for a microanatomical distinction of the *pmfs* from the surrounding MFG. Further, the depth profiles of T_1w/T_2w values within the MFG are similar to classic myeloarchitectural quantifications of the MFG (**Figure 4**).

The pmfs-p, pmfs-i, and pmfs-a exhibit different characteristic patterns of whole brain functional connectivity

To determine if the *pmfs-p*, *pmfs-i*, and *pmfs*-a are functionally distinct, we leveraged detailed individual functional parcellations of the entire cerebral cortex based on functional connectivity from a recently published study (Kong et al., 2018; **Figure 5a**). Importantly, this parcellation was conducted blind to both cortical folding and our sulcal definitions. Within each hemisphere in the same participants in which we generated manual sulcal labels, we generated a functional connectivity network profile (which we refer to as a "connectivity fingerprint"). For each sulcal component, we calculated the overlap between 17 functional networks (on the native hemisphere, based on the DICE coefficient; **Materials and Methods**). This technique generated a cortical topography reflective of the whole-brain connectivity patterns for each sulcal component (**Figure 5a, bottom**), and can be interpreted similarly to other studies of functional network variations (Gordon et al., 2017; Seitzman et al., 2019), as a trait-like connectivity profile for each *pmfs* component within each participant.

[INSERT FIGURE 5 HERE]

Our approach demonstrated that the *pmfs-p*, *pmfs-i*, and *pmfs-a* have different connectivity fingerprints and thus, are functionally dissociable. Average connectivity fingerprints across participants are illustrated in **Figure 5b**. A repeated-measures ANOVA with sulcal component (*pmfs-p*, *pmfs-i*, *pmfs-a*), hemisphere (left, right), and network yielded a significant component x network interaction ($F(32, 1120) = 45.2$, $p < 0.001$, $\eta_G^2 = 0.29$), as well as a component x network x hemisphere interaction ($F(32, 1120) = 5.26$, $p < 0.001$, $\eta_G^2 = 0.040$) (**Figure 5b**). In each hemisphere, there is a component x network interaction (left: $F(32, 1120) = 29.4$, $p < 0.001$, $\eta_G^2 = 0.35$, right:

$F(32, 1120) = 23.2$, $p < 0.001$, $\eta_G^2 = 0.27$) in which the difference between hemispheres is driven by the *pmfs-p* connectivity fingerprint. Specifically, the *pmfs-p* overlaps most with the default mode network in the left hemisphere and the cognitive control network in the right hemisphere.

Additionally, there are also individual and hemispheric differences in the connectivity fingerprint of each *pmfs* component at the level of individual participants (**Figure 5c**; **Extended Data Figure 5-1**). To characterize individual differences, we built on work showing network connectivity variations across individuals (Kong et al., 2018; Seitzman et al., 2019) by relating this connectivity variability to individual anatomical landmarks in LPFC. We quantified connectivity fingerprint variability by measuring the pairwise Wasserstein distance between the connectivity profiles for all unique participant pairs for each sulcal component, in which a larger distance indicates decreased similarity, and therefore greater variability (see **Materials and Methods**). This approach quantifies how variable the pattern of network overlap (connectivity fingerprint) is across individuals for each *pmfs* component (**Figure 5c**, right). In the right hemisphere, the *pmfs-p* showed the most variable network profile across all unique participant pairs (*pmfs-p* vs. *pmfs-i*, Wilcoxson-Signed rank test, $W = 7.2\text{x}10^4$, $p < 0.001$, *pmfs-p* vs. *pmfs-a*, $W = 7.4\text{x}10^4$, $p < 0.001$), while the *pmfs-i* was most variable in the left hemisphere (*pmfs-i* vs. *pmfs-a*, $W = 8.8\text{x}10^4$, $p = 0.014$, *pmfs-i* vs. *pmfs-p*, $W = 8.0\text{x}10^4$, $p < 0.001$). This analysis suggests that the right *pmfs-p* and left *pmfs-i* mark regions of LPFC with particularly high levels of individual differences in functional connectivity profiles, providing an anatomical substrate for network connectivity differences across individuals.

The pmfs-p, pmfs-i, and pmfs-a are functionally dissociable: Meta-analyses across 83 experimental task categories

We next tested if the dissociation of functional networks between the *pmfs-p*, *pmfs-i*, and *pmfs-a* identified in individual participants (**Figure 5**) can also be observed in meta-analytic analyses of functional activation data at the group-level. That is, do the components of the *pmfs* show a functional dissociation of engagement over a wide array of cognitive operations? To test for different patterns of functional activations across tasks, we generated sulcal probability maps on a template cortical surface (**Figure 6a**, bottom left). Analogous to probabilistic maps for functional regions (Wang et al., 2015; Weiner et al., 2017; Weiner et al., 2018), the maps provide a vertex-wise measure of anatomical overlap across individuals for all 13 LPFC sulci examined in the present study. As the *pmfs* components disappear on average templates (**Figure 1**), these probabilistic maps are independent of the sulcal patterning of the template itself, which merely serves as a cortical surface independent of each individual cortical surface. We then compared these sulcal probability maps to 14 probabilistic "cognitive component" maps derived from an author-topic model of meta-analytic activation data across 83 experimental task categories (Yeo et al., 2015).

[INSERT FIGURE 6 HERE]

The cognitive component model links patterns of brain activity to behavioral tasks via latent components representing putative functional subsystems (Yeo et al., 2015). Each cognitive component map (which was calculated on the same template cortical surface used here) provides the probability that a given voxel will be activated by each of the 14 components (across all 83

tasks). We then used an expectation maximization algorithm (via posterior probability, **Materials and Methods**) to relate brain activity in each sulcal probability map to each cognitive component (**Figure 6a**, right). Importantly, when calculating the posterior probabilities, we implemented a leave-one-participant-out cross-validation procedure when constructing the sulcal probability maps in order to assess variability in the generated posterior probabilities for each cognitive component (**Figure 6b**). To indicate feasibility of this approach, the somato-motor components of the cognitive component map (C01, C02) align most highly with the central sulcus as one would expect, which shows the ability of this method to measure structural-functional correspondences at the meta-analytic level.

This approach further reveals that the *pmfs-p*, *pmfs-i*, and *pmfs-a* are functionally dissociable based on meta-analytic data of cognitive task activations. In the right hemisphere, the *pmfs-p*, *pmfs-i*, and *pmfs-a* showed distinct probabilities for separate cognitive components: 1) the *pmfs-p* loaded onto a default mode component (C11), 2) the *pmfs-i* loaded onto an executive function component (C10), and 3) the *pmfs-a* loaded onto an inhibitory control component (C09). In the left hemisphere, the *pmfs-a* and *pmfs-i* both loaded onto an executive function (C10) component, while the *pmfs-p* loaded onto an emotional processing/episodic memory component (C12). The *pmfs* was also dissociable in activation profiles from the more anterior *imfs*. In the left hemisphere, the imfs showed no overlap with the *pmfs*, with the *imfs-h* loading onto the inhibitory control component (C09), and the *imfs-v* loading onto a default mode component (C11). In the right hemisphere, both the *imfs-h and imfs-v* loaded onto the same inhibitory control component (C09) as the *pmfs-a*.

Like our individual participant analyses, there were also hemispheric differences: the cognitive components overlapping the most with the *pmfs-a* and *pmfs-p* differed between the two

563 hemispheres. The *pmfs-p* loaded onto an emotional processing/episodic memory component in
564 the left hemisphere (**Figure 6b**, top row) and a default mode component in the right hemisphere
565 (**Figure 6b**, top row), while the *pmfs-a* loaded onto an executive function component in the left
566 hemisphere (**Figure 6b**, third row) and an inhibitory control component in the right hemisphere
567 (**Figure 6b**, third row).

568 Finally, previous studies have identified retinotopic representations in human LPFC
569 (Hagler and Sereno, 2006; Kastner et al., 2007; Mackey et al., 2017), but the three *pmfs*
570 components did not overlap with cognitive components associated with visual processing in
571 these meta-analytic analyses. To further examine the relationship between the *pmfs* components
572 and visual processing, we analyzed whether the *pmfs* components explained a significant amount
573 of variance (**Figure 7**) in a newly published, whole brain dataset of population receptive field
574 measurements in 181 participants (Benson et al., 2018). When considering voxels that
575 demonstrate retinotopic responses (R^2 > 15%), the highest overlap between predicted *pmfs*
576 location and retinotopic representations was specific to the right hemisphere for the *pmfs-i* (mean
577 R^2 across participants = 28.5%), with less overlap in the left hemisphere (all other *pmfs* R^2 values
578 < 20%). The most consistent correspondence between visual field maps and sulcal location
579 occurred at (1) the intersection of the *sprs* and *sfs-p*, and (2) the intersection of the *iprs* and *ifs*, as
580 previously reported ((Mackey et al., 2017); **Figure 7**). The *iprs* showed the highest retinotopic
581 responses of the LPFC sulci (lh: 34.2%; rh: 48.9%) measured here, and this is also consistent
582 with a recent study identifying a region critical for conditional eye movements within a similar
583 location in the *ifs* (Germann and Petrides, 2020). Future studies examining the relationship
584 between *pmfs* components and retinotopic representations in individual participants will further
585 expand on these findings.

[INSERT FIGURE 7 HERE]

Extensive individual differences in the location of the pmfs across individuals

Although the three *pmfs* components are prominent within each hemisphere, there is extensive individual variability in the precise location of each sulcal component within the posterior MFG. To determine how well the probability maps could predict the location of the *pmfs-p*, *pmfs-i*, and *pmfs-a* within *individual* hemispheres, we used a cross-validated approach, iteratively leaving out one participant from the calculation of probability maps (**Figure 8a**). Then, the maximum probability maps (MPMs) were projected to the held-out individual's native cortical surface to calculate the overlap between the manually identified and probabilistically identified sulcal locations. This procedure resulted in a measure of location variability for each sulcal component (**Figure 8b**). For these calculations, we used the *central sulcus* (*cs*) as a noise ceiling (left: *cs* = 0.85 ± 0.02; right: *cs* = 0.85 ± 0.06) as it is a) considered very stable across individuals (see **Materials and Methods**) and b) used in the cortex-based alignment procedure (Fischl et al., 1999b).

[INSERT FIGURE 8 HERE]

The *pmfs* components exhibited significant variability in sulcal location across participants (left: *pmfs-p* = 0.30 ± 0.28, *pmfs-i* = 0.32 ± 0.18, *pmfs-a* = 0.27 ± 0.20; right: *pmfs-p* = 0.03 ± 0.04, *pmfs-i* = 0.37 ± 0.18, *pmfs-a* = 0.20 ± 0.20). A 2-way repeated-measures ANOVA with *pmfs* sulcal component (*pmfs-p*, *pms-i*, *pmfs-a*) and hemisphere (*right*, *left*) revealed a sulcus x hemisphere interaction ($F(1.84, 64.47) = 9.52$, $p < 0.001$, $\eta^2_G = 0.08$) driven by the finding that the *pmfs-p* is highly variable across individuals, resulting in very little predictability in the right hemisphere (**Figure 8b**). When using all three *pmfs* components together, prediction is more robust (left: *pmfs* = 0.41 ± 0.13; right: *pmfs* = 0.37 ±

608 0.15), but still much lower than the predictability of the *cs* and also lower than prediction
609 performance for all other LPFC sulci quantified in the present study (**Figure 8b**). These results
610 demonstrate that although the *pmfs* is prominent within each individual (**Extended Data Figure**
611 **2-1**), the location of each *pmfs* component is variable across individuals, which provides
612 empirical support for the historical confusion regarding its identification and labeling (**Figure 1**).

613

614

Discussion

Here, we examined the relationship between cortical anatomy and function in human lateral prefrontal cortex (LPFC) and showed for the first time (to our knowledge) that the posterior middle frontal sulcus (*pmfs*) serves as a meso-scale link between myelin content and functional connectivity in individual participants. The *pmfs* is a characteristically shallow tertiary sulcus with three components that differ in their myelin content, resting state connectivity profiles, and engagement across meta-analyses of 83 cognitive tasks. We first discuss how these findings suggest modern empirical support for a classic, yet largely unconsidered, anatomical theory (Sanides, 1962, 1964), as well as a recent cognitive neuroscience theory proposing a functional hierarchy in LPFC (Koechlin and Summerfield, 2007; Badre and D'Esposito, 2009; Badre and Nee, 2018). We end by discussing a growing need for computational tools that automatically define tertiary sulci throughout cortex.

The anatomical-functional coupling in LPFC identified here is quite surprising considering the widespread literature providing little support for fine-grained anatomical-functional coupling in this cortical expanse and in association cortices more broadly when conducting traditional group-analyses (Paquola et al., 2019; Vazquez-Rodriguez et al., 2019). Indeed, cortical folding patterns relative to the location of anatomical, functional, or multimodal transitions are considered “imperfectly correlated” (Welker, 1990; Glasser et al., 2016) in association cortices and especially in LPFC (Van Essen et al., 2012; Caspers et al., 2013; Robinson et al., 2014; Coalson et al., 2018). Contrary to these previous findings that did not consider tertiary sulci, the present findings appear to support a classic, yet largely unconsidered theory proposed by Sanides (1962, 1964) that tertiary sulci are potentially meaningful anatomical and functional landmarks in association cortices – and in particular, in LPFC. Specifically,

638 Sanides proposed that because tertiary sulci emerge late in gestation and exhibit a protracted
639 postnatal development, they likely serve as functional and architectonic landmarks in human
640 association cortices, which also exhibit a protracted postnatal development. Sanides (1964)
641 further proposed that the late morphological development of tertiary sulci is likely related to
642 protracted cognitive skills associated with LPFC. Interestingly, identifying *pmfs* components in
643 his classic images shows myeloarchitectonic gradations among five areas in LPFC (**Figure 9a**).
644 Linking these data to recent modern parcellations of the human cerebral cortex (Sallet et al.,
645 2013; Glasser et al., 2016) shows that *pmfs* components likely serve as boundaries among a
646 series of cortical areas, which can be addressed in future research in individual participants
647 (**Figure 9b**).

648 **[INSERT FIGURE 9 HERE]**

649 In addition to supporting Sanides' classic anatomical theory, the present data
650 demonstrated that the three *pmfs* components exhibit different resting-state connectivity profiles
651 along a rostral-caudal axis, which builds on previous work also supporting a functional hierarchy
652 along a rostral-caudal axis of LPFC. Further consistent with this hierarchy, evidence from
653 neuroimaging, lesion, and electrocorticography studies indicate that this proposed rostral-caudal
654 axis of LPFC is also related to levels of temporal and cognitive abstraction. That is, more
655 anterior LPFC cortical regions are more highly engaged in tasks with higher abstract complexity
656 (Koechlin et al., 2003; Koechlin and Summerfield, 2007; Voytek et al., 2015; Mansouri et al.,
657 2017). While there is axonal tracing data in non-human primates suggesting an anatomical basis
658 for such a hierarchical organization (Goulas et al., 2014; Goulas et al., 2019), the present
659 findings provide new evidence for anatomically and functionally dissociable sulcal components
660 in LPFC that also support a hierarchical organization within individuals. Future work leveraging

finer-scale multimodal and microanatomical data from individual human brains will be critical for uncovering anatomical and functional properties of LPFC across spatial and temporal scales that may further support the proposed functional rostral-caudal hierarchy of human LPFC.

Together, the culmination of present and previous findings suggest that tertiary sulci are landmarks in human ventral temporal cortex (Nasr et al., 2011; Caspers et al., 2013; Weiner et al., 2014; Lorenz et al., 2017), medial PFC (Amiez et al., 2019; Lopez-Persem et al., 2019), and now, LPFC. This begs the question: How many other tertiary sulci serve as cortical landmarks? We stress that it is unlikely that all tertiary sulci will serve as cortical landmarks, since neuroanatomists have known for over a century that not all sulci function as cortical landmarks (Smith, 1907; Bailey and Bonin, 1951; Ono et al., 1990; Welker, 1990; Van Essen et al., 2019). Nonetheless, this does not preclude the importance of future studies identifying which tertiary sulci are architectonic, functional, behavioral, or multimodal landmarks – not only in healthy young adults as examined here, but also in developmental (Voorhies et al., 2020) and clinical (Garrison et al., 2015; Brun et al., 2016) cohorts. Additionally, tertiary sulci can also serve as evolutionary markers for primate cortical homology. For example, shallow “dimples” co-occur with the frontal eye field (FEF) in macaques, while deeper sulci co-occur with the proposed homologue of the FEF in humans (Amiez and Petrides, 2009; Schall et al., 2020). Humans may also have tertiary sulci in locations that non-human primates do not have dimples as was recently shown in medial PFC (Amiez et al., 2019).

Carefully examining the relationship among tertiary sulci and multiple types of anatomical, functional, and behavioral data in individual participants will require new neuroimaging tools to automatically identify tertiary sulci throughout human cortex. For instance, most neuroimaging software packages are only capable of automatically defining ~30-

35 primary and secondary sulci in a given hemisphere (Destrieux et al., 2010). Current estimates approximate ~110 sulci in each hemisphere when considering tertiary sulci (Petrides, 2019). Thus, studies in the immediate future will still require the manual identification of tertiary sulci, which is labor intensive and requires expertise ((Miller et al., 2020a) for a historical discussion regarding the manual labeling of tertiary sulci in LPFC). For example, the present study required manual definitions of 936 sulci in 72 hemispheres. While 72 is a large sample size compared to other labor-intensive anatomical studies in which 20 hemispheres is considered sufficient to encapsulate individual differences (Amunts and Zilles, 2015; Amunts et al., 2020), 2400 hemispheres are available just from the HCP alone. Defining tertiary sulci in only the LPFC of every HCP participant would require ~26,400 manual definitions, while defining all tertiary sulci in the entire HCP dataset would require over a quarter of a million (~256,800) manual definitions. Consequently, manual identification of tertiary sulci will continue to limit sample sizes in immediate future studies until new automated methods are generated (Klein et al., 2017; Hao et al., 2020; Lyu et al., 2020).

In the interim, we sought to leverage the anatomical labeling in this study to aid the field in the identification of sulcal landmarks in LPFC. The probability maps of sulcal locations in the present study are openly available and may be transformed to held-out individual brains (**Figure 9**). Accordingly, manual identification of these landmarks within individuals is greatly aided, allowing future studies to apply these tools to identify LPFC tertiary in individual participants, including those from various groups such as patient or developmental cohorts. Because smaller tertiary sulci in association cortex are the latest sulcal indentations to develop (Sanides, 1962, 1964; Chi et al., 1977; Welker, 1990; Armstrong et al., 1995), their anatomical trajectories and properties likely relate to the development of cognitive abilities associated with the LPFC and

other association areas as Sanides hypothesized, which recent ongoing work supports (Voorhies et al., 2020). Moving forward, we hope to leverage the manual labeling performed here to develop better automated algorithms for sulcal labeling within individuals. Future work using deep learning algorithms may help to identify tertiary structures in novel brains without manual labeling or intervention (Borne et al., 2020; Hao et al., 2020; Lyu et al., 2020). Such automated tools have translational applications as tertiary sulci are largely hominoid-specific structures (Amiez et al., 2019; Miller et al., 2020b) located in association cortices associated with pathology in many neurological disorders. Thus, morphological features of these under-studied neuroanatomical structures may be useful clinical biomarkers for future diagnostic purposes. To begin to achieve this goal and to aid the field, we share our probabilistic maps of LPFC tertiary sulci with the publication of this paper.

720
721 **Data availability**

722 Data were provided by the Human Connectome Project, WU-Minn Consortium (Principal
723 Investigators: David Van Essen and Kamil Ugurbil; 1U54MH091657) funded by the 16 NIH
724 Institutes and Centers that support the NIH Blueprint for Neuroscience Research; and by the
725 McDonnell Center for Systems Neuroscience at Washington University. The HCP dataset and
726 processing are described in previous publications (Glasser et al., 2013; Glasser et al., 2016). The
727 probability maps for LPFC sulcal definitions and analysis code will be freely available with the
728 publication of the paper on Open Science Framework (OSF).

729

730
731 **Author Contributions**

732 Manual anatomical labeling: J.A.M., W.V., K.S.W. Data analysis and interpretation of the data:
733 J.A.M., D.J.L., K.S.W. Drafting paper: J.A.M, K.S.W. Revising paper: J.A.M, W.V., D.J.L.,
734 M.D., K.S.W. Supervision and study conceptualization: J.A.M., M.D, K.S.W.

735

736 **Acknowledgments**

737 This work was supported by (1) start-up funds provided by the University of California,
738 Berkeley and the Helen Wills Neuroscience Institute (K.S.W.); (2) NIH grant RO1 MH63901
739 (J.A.M., M.D.). We also thank Jewelia Yao for help with the manual definition of LPFC sulci.

740

741
742
743
744
745
746

747

References

Amiez C, Petrides M (2007) Selective involvement of the mid-dorsolateral prefrontal cortex in the coding of the serial order of visual stimuli in working memory. Proc Natl Acad Sci U S A 104:13786-13791.

Amiez C, Petrides M (2009) Anatomical organization of the eye fields in the human and non-human primate frontal cortex. Prog Neurobiol 89:220-230.

Amiez C, Sallet J, Hopkins WD, Meguerditchian A, Hadj-Bouziane F, Ben Hamed S, Wilson CRE, Procyk E, Petrides M (2019) Sulcal organization in the medial frontal cortex provides insights into primate brain evolution. Nat Commun 10:3437.

Amunts K, Zilles K (2015) Architectonic Mapping of the Human Brain beyond Brodmann. Neuron 88:1086-1107.

Amunts K, Mohlberg H, Bludau S, Zilles K (2020) Julich-Brain: A 3D probabilistic atlas of the human brain's cytoarchitecture. Science 369:988-992.

Annese J, Pitiot A, Dinov ID, Toga AW (2004) A myelo-architectonic method for the structural classification of cortical areas. Neuroimage 21:15-26.

Armstrong E, Schleicher A, Heyder O, Maria C, Zilles K (1995) The Ontogeny of Human Gyrification. Cereb Cortex 5.

Badre D, D'Esposito M (2009) Is the rostro-caudal axis of the frontal lobe hierarchical? Nat Rev Neurosci 10:659-669.

Badre D, Nee DE (2018) Frontal Cortex and the Hierarchical Control of Behavior. Trends Cogn Sci 22:170-188.

Bailey P, Bonin GV (1951) The Isocortex of Man. Urbana: University of Illinois Press.

Barrett RLC, Dawson M, Dyrby TB, Krug K, Ptito M, D'Arceuil H, Croxson PL, Johnson PJ, Howells H, Forkel SJ, Dell'Acqua F, Catani M (2020) Differences in Frontal Network Anatomy Across Primate Species. J Neurosci 40:2094-2107.

Benson NC, Jamison KW, Arcaro MJ, Vu AT, Glasser MF, Coalson TS, Van Essen DC, Yacoub E, Ugurbil K, Winawer J, Kay K (2018) The Human Connectome Project 7 Tesla retinotopy dataset: Description and population receptive field analysis. J Vis 18:23.

Borne L, Riviere D, Mancip M, Mangin JF (2020) Automatic labeling of cortical sulci using patch- or CNN-based segmentation techniques combined with bottom-up geometric constraints. Med Image Anal 62:101651.

Braitenberg V (1962) A note on myeloarchitectonics. J Comp Neurol 118:141-156.

Brun L, Auzias G, Viellard M, Villeneuve N, Girard N, Poinso F, Da Fonseca D, Deruelle C (2016) Localized Misfolding Within Broca's Area as a Distinctive Feature of Autistic Disorder. Biol Psychiatry Cogn Neurosci Neuroimaging 1:160-168.

Caspers J, Zilles K, Eickhoff SB, Schleicher A, Mohlberg H, Amunts K (2013) Cytoarchitectonical analysis and probabilistic mapping of two extrastriate areas of the human posterior fusiform gyrus. Brain Struct Funct 218:511-526.

Chi JG, Dooling EC, Gilles FH (1977) Gyral development of the human brain. Ann Neurol 1:86-93.

Coalson TS, Van Essen DC, Glasser MF (2018) The impact of traditional neuroimaging methods on the spatial localization of cortical areas. Proc Natl Acad Sci U S A 115:E6356-E6365.

Connolly C (1950) External Morphology of the Primate Brain. Springfield.

793 Dale AM, Fischl B, Sereno MI (1999) Cortical surface-based analysis. I. Segmentation and
794 surface reconstruction. Neuroimage 9:179-194.
795 Demirtas M, Burt JB, Helmer M, Ji JL, Adkinson BD, Glasser MF, Van Essen DC, Sotiropoulos
796 SN, Anticevic A, Murray JD (2019) Hierarchical Heterogeneity across Human Cortex
797 Shapes Large-Scale Neural Dynamics. Neuron 101:1181-1194 e1113.
798 Destrieux C, Fischl B, Dale A, Halgren E (2010) Automatic parcellation of human cortical gyri
799 and sulci using standard anatomical nomenclature. Neuroimage 53:1-15.
800 Dick F, Tierney AT, Lutti A, Josephs O, Sereno MI, Weiskopf N (2012) In vivo functional and
801 myeloarchitectonic mapping of human primary auditory areas. J Neurosci 32:16095-
802 16105.
803 Ding SL et al. (2016) Comprehensive cellular-resolution atlas of the adult human brain. J Comp
804 Neurol 524:3127-3481.
805 Donahue CJ, Glasser MF, Preuss TM, Rilling JK, Van Essen DC (2018) Quantitative assessment
806 of prefrontal cortex in humans relative to nonhuman primates. Proc Natl Acad Sci U S A.
807 Eberstaller O (1890) Das Stirnhirn. Wien: Urban & Schwarzenberg.
808 Fischl B, Sereno MI, Dale AM (1999a) Cortical surface-based analysis. II: Inflation, flattening,
809 and a surface-based coordinate system. Neuroimage 9:195-207.
810 Fischl B, Sereno MI, Tootell RBH, Dale AM (1999b) High-Resolution Intersubject Averaging
811 and a Coordinate System for the Cortical Surface. Human Brain Mapping 8:272-284.
812 Fisher AV (2019) Selective sustained attention: a developmental foundation for cognition.
813 Current Opinion in Psychology 29:248-253.
814 Flechsig P (1920) Anatomie des Menschlichen Gehirns und Rückenmarks auf Myelogenetischer
815 Grundlage. Leipzig.
816 Fritz CO, Morris PE, Richler JJ (2012) Effect size estimates: current use, calculations, and
817 interpretation. J Exp Psychol Gen 141:2-18.
818 Gao JS, Huth AG, Lescroart MD, Gallant JL (2015) Pycortex: an interactive surface visualizer
819 for fMRI. Front Neuroinform 9:23.
820 Garrison JR, Fernyhough C, McCarthy-Jones S, Haggard M, Australian Schizophrenia Research
821 B, Simons JS (2015) Paracingulate sulcus morphology is associated with hallucinations
822 in the human brain. Nat Commun 6:8956.
823 Germann J, Petrides M (2020) Area 8A within the Posterior Middle Frontal Gyrus Underlies
824 Cognitive Selection between Competing Visual Targets. eNeuro 7.
825 Glasser MF, Van Essen DC (2011) Mapping human cortical areas in vivo based on myelin
826 content as revealed by T1- and T2-weighted MRI. J Neurosci 31:11597-11616.
827 Glasser MF, Coalson TS, Robinson EC, Hacker CD, Harwell J, Yacoub E, Ugurbil K, Andersson
828 J, Beckmann CF, Jenkinson M, Smith SM, Van Essen DC (2016) A multi-modal
829 parcellation of human cerebral cortex. Nature 536:171-178.
830 Glasser MF, Sotiropoulos SN, Wilson JA, Coalson TS, Fischl B, Andersson JL, Xu J, Jbabdi S,
831 Webster M, Polimeni JR, Van Essen DC, Jenkinson M, Consortium WU-MH (2013) The
832 minimal preprocessing pipelines for the Human Connectome Project. Neuroimage
833 80:105-124.
834 Gordon EM, Laumann TO, Gilmore AW, Newbold DJ, Greene DJ, Berg JJ, Ortega M, Hoyt-
835 Drazen C, Gratton C, Sun H, Hampton JM, Coalson RS, Nguyen AL, McDermott KB,
836 Shimony JS, Snyder AZ, Schlaggar BL, Petersen SE, Nelson SM, Dosenbach NUF
837 (2017) Precision Functional Mapping of Individual Human Brains. Neuron.

838 Goulas A, Uylings HB, Stiers P (2014) Mapping the hierarchical layout of the structural network
839 of the macaque prefrontal cortex. Cereb Cortex 24:1178-1194.
840 Goulas A, Majka P, Rosa MGP, Hilgetag CC (2019) A blueprint of mammalian cortical
841 connectomes. PLoS Biol 17:e2005346.
842 Hagler DJ, Jr., Sereno MI (2006) Spatial maps in frontal and prefrontal cortex. Neuroimage
843 29:567-577.
844 Hao L, Bao S, Tang Y, Gao R, Parvathaneni P, Miller JA, Voorhies W, Yao J, Bunge SA,
845 Weiner KS, Landman BA, Lyu I (2020) Automatic Labeling of Cortical Sulci using
846 Convolutional Neural Networks in a Developmental Cohort. In: IEEE International
847 Symposium on Biomedical Imaging (ISBI). Iowa City, IA.
848 Hinds OP, Rajendran N, Polimeni JR, Augustinack JC, Wiggins G, Wald LL, Diana Rosas H,
849 Potthast A, Schwartz EL, Fischl B (2008) Accurate prediction of V1 location from
850 cortical folds in a surface coordinate system. Neuroimage 39:1585-1599.
851 Hopf A (1956) Über die Verteilung myeloarchitektonischer Merkmale in der Stirnhirnrinde beim
852 Menschen. J Hirnforsch 2:311-333.
853 Kastner S, DeSimone K, Konen CS, Szczepanski SM, Weiner KS, Schneider KA (2007)
854 Topographic maps in human frontal cortex revealed in memory-guided saccade and
855 spatial working-memory tasks. J Neurophysiol 97:3494-3507.
856 Klein A, Ghosh SS, Bao FS, Giard J, Hame Y, Stavsky E, Lee N, Rossa B, Reuter M, Chaibub
857 Neto E, Keshavan A (2017) Mindboggling morphometry of human brains. PLoS Comput
858 Biol 13:e1005350.
859 Koechlin E, Summerfield C (2007) An information theoretical approach to prefrontal executive
860 function. Trends Cogn Sci 11:229-235.
861 Koechlin E, Ody C, Kouneiher F (2003) The architecture of cognitive control in the human
862 prefrontal cortex. Science 302:1181-1185.
863 Kong R, Li J, Orban C, Sabuncu MR, Liu H, Schaefer A, Sun N, Zuo XN, Holmes AJ, Eickhoff
864 SB, Yeo BTT (2018) Spatial Topography of Individual-Specific Cortical Networks
865 Predicts Human Cognition, Personality, and Emotion. Cereb Cortex.
866 Lopez-Persem A, Verhagen L, Amiez C, Petrides M, Sallet J (2019) The Human Ventromedial
867 Prefrontal Cortex: Sulcal Morphology and Its Influence on Functional Organization. J
868 Neurosci 39:3627-3639.
869 Lorenz S, Weiner KS, Caspers J, Mohlberg H, Schleicher A, Bludau S, Eickhoff SB, Grill-
870 Spector K, Zilles K, Amunts K (2017) Two New Cytoarchitectonic Areas on the Human
871 Mid-Fusiform Gyrus. Cereb Cortex 27:373-385.
872 Lyu I, Bao S, Hao L, Yao J, Miller JA, Voorhies W, Taylor WD, Bunge SA, Weiner KS,
873 Landman BA (2020) Labeling Lateral Prefrontal Sulci using Spherical Data
874 Augmentation and Context-aware Training. Neuroimage (in revision).
875 Mackey WE, Winawer J, Curtis CE (2017) Visual field map clusters in human frontoparietal
876 cortex. Elife 6.
877 Madan CR (2019) Robust estimation of sulcal morphology. Brain Inform 6:5.
878 Mansouri FA, Koechlin E, Rosa MGP, Buckley MJ (2017) Managing competing goals - a key
879 role for the frontopolar cortex. Nat Rev Neurosci 18:645-657.
880 Miller EK, Cohen JD (2001) AN INTEGRATIVE THEORY OF PREFRONTAL CORTEX
881 FUNCTION. Annu Rev Neurosci 24:167-202.
882 Miller JA, D'Esposito M, Weiner KS (2020a) Using tertiary sulci to map the "cognitive globe"
883 of prefrontal cortex. psyArxiv.

884 Miller JA, Voorhies WI, Li X, Raghuram I, Palomero-Gallagher N, Zilles K, Sherwood CC,
885 Hopkins WD, Weiner KS (2020b) Sulcal morphology of ventral temporal cortex is
886 shared between humans and other hominoids. Sci Rep 10:17132.
887 Nasr S, Liu N, Devaney KJ, Yue X, Rajimehr R, Ungerleider LG, Tootell RB (2011) Scene-
888 selective cortical regions in human and nonhuman primates. J Neurosci 31:13771-13785.
889 Nee DE, D'Esposito M (2016) The hierarchical organization of the lateral prefrontal cortex.
890 eLife 5.
891 Ono M, Kubik S, Abernathey C (1990) Atlas of the Cerebral Sulci. New York: Thieme Medical
892 Publishers, Inc.
893 Paquola C, Vos De Wael R, Wagstyl K, Bethlehem RAI, Hong SJ, Seidlitz J, Bullmore ET,
894 Evans AC, Misic B, Margulies DS, Smallwood J, Bernhardt BC (2019) Microstructural
895 and functional gradients are increasingly dissociated in transmodal cortices. PLoS Biol
896 17:e3000284.
897 Petrides M (2019) Atlas of the Morphology of the Human Cerebral Cortex on the Average MNI
898 Brain, 1 Edition. London, UK: Elsevier.
899 Petrides M, Pandya DN (2012) The-Frontal-Cortex. In: The Human Nervous System (Mai J,
900 Paxinos G, eds), pp 988-1011: Elsevier.
901 Rajkowska G, Goldman-Rakic PS (1995) Cytoarchitectonic Definition of Prefrontal areas in the
902 Normal Human Cortex: II. Variability in Locations of Areas 9 and 46 and Relationship to
903 the Talairach Coordinate System. Cereb Cortex 5.
904 Retzius G (1896) Das Menschenhirn. Stockholm, Sweden: Norstedt and Soener.
905 Robinson EC, Jbabdi S, Glasser MF, Andersson J, Burgess GC, Harms MP, Smith SM, Van
906 Essen DC, Jenkinson M (2014) MSM: a new flexible framework for Multimodal Surface
907 Matching. Neuroimage 100:414-426.
908 Rollins CPE, Garrison JR, Arribas M, Seyedsalehi A, Li Z, Chan RCK, Yang J, Wang D, Lio P,
909 Yan C, Yi ZH, Cachia A, Upthegrove R, Deakin B, Simons JS, Murray GK, Suckling J
910 (2020) Evidence in cortical folding patterns for prenatal predispositions to hallucinations
911 in schizophrenia. Transl Psychiatry 10:387.
912 Rowley CD, Bazin PL, Tardif CL, Sehmbi M, Hashim E, Zaharieva N, Minuzzi L, Frey BN,
913 Bock NA (2015) Assessing intracortical myelin in the living human brain using
914 myelinated cortical thickness. Front Neurosci 9:396.
915 Sallet J, Mars RB, Noonan MP, Neubert FX, Jbabdi S, O'Reilly JX, Filippini N, Thomas AG,
916 Rushworth MF (2013) The organization of dorsal frontal cortex in humans and
917 macaques. J Neurosci 33:12255-12274.
918 Sanides F (1962) Die Architektonik Des Menschlichen Stirnhirns Zugleich Eine Darstellung Der
919 Prin. In: Monographien aus dem Gesamtgebiete der Neurologie und Psychiatrie (Muller
920 M, Spatz H, Vogel P, eds), pp 176-190. Berlin: Springer Berlin Heidelberg.
921 Sanides F (1964) STRUCTURE AND FUNCTION OF THE HUMAN FRONTAL LOBE.
922 Neuropsychologia 2:209-219.
923 Sanides F (1972) Representation in the cerebral cortex and its areal lamination patterns. In: The
924 Structure and Function of Nervous Tissue (Bourne GH, ed), pp 329-453. New York:
925 Academic Press.
926 Schall JD, Zinke W, Cosman JD, Schall MS, Pare M, Pouget P (2020) On the Evolution of the
927 Frontal Eye Field: Comparisons of Monkeys, Apes, and Humans. In: Evolutionary
928 Neuroscience, 2 Edition (Kaas JH, ed), pp 861-883: Elsevier.

929 Seitzman BA, Gratton C, Laumann TO, Gordon EM, Adeyemo B, Dworetsky A, Kraus BT,
930 Gilmore AW, Berg JJ, Ortega M, Nguyen A, Greene DJ, McDermott KB, Nelson SM,
931 Lessov-Schlaggar CN, Schlaggar BL, Dosenbach NUF, Petersen SE (2019) Trait-like
932 variants in human functional brain networks. Proc Natl Acad Sci U S A 116:22851-
933 22861.
934 Semendeferi K, Lu A, Schenker N, Damasio H (2002) Humans and great apes share a large
935 frontal cortex. Nat Neurosci 5:272-276.
936 Shams Z, Norris DG, Marques JP (2019) A comparison of in vivo MRI based cortical myelin
937 mapping using T1w/T2w and R1 mapping at 3T. PLoS One 14:e0218089.
938 Smith GE (1907) A New Topographical Survey of the Human Cerebral Cortex, being an
939 Account of the Distribution of the Anatomically Distinct Cortical Areas and their
940 Relationship to the Cerebral Sulci. J Anat Physiol 41:237-254.
941 Szczepanski SM, Knight RT (2014) Insights into human behavior from lesions to the prefrontal
942 cortex. Neuron 83:1002-1018.
943 Van Essen DC, Dierker DL (2007) Surface-based and probabilistic atlases of primate cerebral
944 cortex. Neuron 56:209-225.
945 Van Essen DC, Glasser MF, Dierker DL, Harwell J (2012) Cortical parcellations of the macaque
946 monkey analyzed on surface-based atlases. Cereb Cortex 22:2227-2240.
947 Van Essen DC, Donahue CJ, Coalson TS, Kennedy H, Hayashi T, Glasser MF (2019) Cerebral
948 cortical folding, parcellation, and connectivity in humans, nonhuman primates, and mice.
949 Proc Natl Acad Sci U S A.
950 Vazquez-Rodriguez B, Suarez LE, Markello RD, Shafiei G, Paquola C, Hagmann P, van den
951 Heuvel MP, Bernhardt BC, Spreng RN, Misic B (2019) Gradients of structure-function
952 tethering across neocortex. Proc Natl Acad Sci U S A 116:21219-21227.
953 Vogt C, Vogt O (1919) Allgemeinere ergebnisse unserer hirnforschung. J Psychol Neurol
954 25:279-462.
955 Voorhies W, Miller JA, Yao J, Bunge SA, Weiner KS (2020) Cognitive insights from
956 evolutionarily new brain structures in prefrontal cortex. bioRxiv.
957 Voytek B, Kayser AS, Badre D, Fegen D, Chang EF, Crone NE, Parvizi J, Knight RT,
958 D'Esposito M (2015) Oscillatory dynamics coordinating human frontal networks in
959 support of goal maintenance. Nat Neurosci 18:1318-1324.
960 Waehnert MD, Dinse J, Weiss M, Streicher MN, Waehnert P, Geyer S, Turner R, Bazin PL
961 (2014) Anatomically motivated modeling of cortical laminae. Neuroimage 93 Pt 2:210-
962 220.
963 Wang L, Mruczek RE, Arcaro MJ, Kastner S (2015) Probabilistic Maps of Visual Topography in
964 Human Cortex. Cereb Cortex 25:3911-3931.
965 Weiner KS, Natu VS, Grill-Spector K (2018) On object selectivity and the anatomy of the
966 human fusiform gyrus. Neuroimage 173:604-609.
967 Weiner KS, Golarai G, Caspers J, Chuapoco MR, Mohlberg H, Zilles K, Amunts K, Grill-
968 Spector K (2014) The mid-fusiform sulcus: a landmark identifying both cytoarchitectonic
969 and functional divisions of human ventral temporal cortex. Neuroimage 84:453-465.
970 Weiner KS, Barnett MA, Lorenz S, Caspers J, Stigliani A, Amunts K, Zilles K, Fischl B, Grill-
971 Spector K (2017) The Cytoarchitecture of Domain-specific Regions in Human High-level
972 Visual Cortex. Cereb Cortex 27:146-161.
973 Welker W (1990) Why does cerebral cortex fissure and fold? A review of determinants of gyri
974 and sulci. In: (Peters A, Jones EG, eds), pp 3-136. New York: Plenum Press.

975 Yeo BT, Krienen FM, Eickhoff SB, Yaakub SN, Fox PT, Buckner RL, Asplund CL, Chee MW
976 (2015) Functional Specialization and Flexibility in Human Association Cortex. Cereb
977 Cortex 25:3654-3672.
978 Yeo BT, Krienen FM, Sepulcre J, Sabuncu MR, Lashkari D, Hollinshead M, Roffman JL,
979 Smoller JW, Zollei L, Polimeni JR, Fischl B, Liu H, Buckner RL (2011) The
980 organization of the human cerebral cortex estimated by intrinsic functional connectivity. J
981 Neurophysiol 106:1125-1165.
982 Zilles K, Palomero-Gallagher N, Amunts K (2013) Development of cortical folding during
983 evolution and ontogeny. Trends Neurosci 36:275-284.
984

Figure Legends

Figure 1. A synopsis of ambiguity regarding sulcal definitions in the human posterior middle frontal gyrus over the last 130 years. Classic and modern schematics of the sulcal patterning in human lateral prefrontal cortex (LPFC). (**a**) Sulci in the middle frontal gyrus are labeled in yellow on classic and modern schematics of human LPFC. Historically, anatomists had previously either (1) not labeled the sulci within the location of the modern *pmfs* (first two images; arrow indicates depicted, but unlabeled sulcal components) (Eberstaller, 1890; Connolly, 1950) or 2) included these sulci in the definition of the posterior portion of the frontomarginal sulcus (third image; (Rajkowska and Goldman-Rakic, 1995)). The most recent schematic (fourth image, **adapted from Petrides, 2019**) proposes that the *pmfs* is separate from the intermediate frontal sulcus (*imfs-h and imfs-v*, synonymous with the *frontomarginal sulcus*) and consists of three distinct components: posterior (*pmfs-p*), intermediate (*pmfs-i*), and anterior (*pmfs-a*). (**b**) Three individually labeled left hemispheres with the *pmfs* outlined in white. The *pmfs* is prominent within individual participants (**Extended Data Figure 2-1** for all participants). The superior and inferior frontal sulci (*sfs, ifs*) are labeled for reference above and below the middle frontal gyrus, respectively. (**c**) Average cortical surfaces show much smaller *pmfs* components compared to individual participants. As more participants are averaged together into templates, the *pmfs* disappears almost entirely, which is inconsistent with their prominence in individual hemispheres.

Figure 2. LPFC tertiary sulci are easily identifiable and characteristically shallow. (**a**) *Left:* an example inflated cortical surface of an individual left hemisphere in which the sulci examined in the present study are outlined and labeled (**Extended Data Figure 2-1** for all participants). Sulci are dark gray, while gyri are light gray. *Right:* Two post-mortem hemispheres (Retzius, 1896) and three histological sections (note that the pmfs components are referred to as "intermediate frontal sulcus" in the Allen Human Brain Atlas: https://atlas.brain-map.org/; (Ding et al., 2016)) showing that the *pmfs* sulci are also identifiable in post-mortem tissue samples**.** (**b**) Top: Surface area for each sulcus (ordered posterior to anterior) is plotted for each individual participant (gray circles), as well as the mean (colored bars) and 95% confidence interval (black line). Acronyms used for each LPFC sulcus are also included. Darker shades indicate right hemisphere values, while lighter shades indicate left hemisphere values. The three *pmfs* sulci have the smallest surface area of all LPFC sulci measured in the present study. Bottom: Same layout as above, but for sulcal depth (mm). The three *pmfs* sulci are the shallowest of the LPFC sulci measured here.

Table 1.
Most common intersections of the *pmfs* components (morphological types).

Table 2.
Surface area and depth of the three *pmfs* components.

Figure 3. The *pmfs* sulci are anatomically differentiable based on myelin content. (**a**) Top: Schematic of the calculation of geodesic distance along the cortical surface. For each sulcus, the average distance of each vertex from the central sulcus was calculated (dotted black line; **Materials and Methods**). Bottom: an example T_1w/T_2w map in an individual participant in which 5-95% percentile of values are depicted. (**b**) T_1w/T_2w values (a proxy for myelin content) are plotted for each component of the *pmfs* for each individual participant (N = 36). Bars represent mean ± 95% CI, while each participant is depicted as a circle. Darker shades indicate right hemisphere values, while lighter shades indicate left hemisphere values. The components of the *pmfs* are differentiable based on myelin content, with a decrease from posterior to anterior across both hemispheres. (**c**) Scatterplot showing the negative relationship between distance from the central sulcus and the mean myelination value for all labeled sulci from each individual

(N = 36 participants). The mixed linear model (**Materials and Methods**) with predictors of distance and hemisphere shows a marginal r^2 of 60.8%. Scatterplot is bootstrapped at 68% CI for visualization. (**d**) Scatterplot showing the mean T_1w/T_2w value for each sulcus as a function of distance (mm) from the central sulcus. Error bars for both the x- and y-axes represent S.E.M. (68% CI) across individuals (N = 36 participants). *Dark purple*: right hemisphere; *Light purple*: left hemisphere.

Figure 4. The *pmfs* sulci and middle frontal gyrus have differentiable myelin profiles across cortical depths. (**a**) Left: Tissue contrast enhancement (T_1w/T_2w metric, a proxy for myelin) at nine cortical depths, sampled from the outer gray matter (*pial*) to the gray/white matter boundary (*white matter*) using equivolume surfaces (**Materials and Methods**). The MFG (excluding the *pmfs*) has higher myelin content than all *pmfs* components in the upper cortical layers, while the *pmfs* components have higher myelin content in deeper layers. Shaded area represents bootstrapped 68% CI across participants. Green asterisks show significant statistical differences between the MFG and all *pmfs* components (MFG > *pmfs*), while purple asterisks show the reverse (*pmfs* > MFG; all tests FWE-corrected at $p < 0.05/9$). Right: Myelinated fiber density (y-axis) profile across cortical depths (x-axis) in post-mortem histological sections of the MFG, adapted from Braitenberg (1962). B: stria of Baillarger. G: stria of Gennari. Similar to our measurements, myelination increases from outer to inner layers within the MFG. (**b**) Left: Individual left hemisphere with the manually defined *pmfs* components (white) and the surrounding MFG (green) as defined by FreeSurfer (Destrieux et al., 2010). We excluded the *pmfs* components from the MFG to test for anatomically distinct profiles. Middle: Example equivolume surfaces at five different cortical depths, from the *pial* to *white matter* surfaces, which were used to sample the T_1w/T_2w metric across depths. Right: Myelination stain of a post-mortem histological section of the MFG from Braitenberg (1962). Arrow: Location from which the myelinated fiber density profile in (**a**, right) was calculated.

Figure 5. The *pmfs* components are functionally differentiable based on connectivity fingerprints within individuals. (**a**) Schematic of how individual-level resting state connectivity profiles were generated in each participant. Resting-state network parcellations for each participant were obtained from a recent study (Kong et al., 2018) in an observer-independent fashion of sulcal definitions in LPFC. Example individual cortical topographies are shown in four individual participants, colored according to the group parcellation. The individual cortical topographies and *pmfs* sulcal definitions were used to calculate the connectivity fingerprint, which represents the overlap of each network within the *pmfs* component of each participant. (**b**) Polar plots showing the mean connectivity fingerprint of the three *pmfs* components (plotted outwards) with each of 17 resting-state functional connectivity networks, across participants. Resting-state networks with the highest overlap across participants are labeled. (**c**) Left: Polar plots showing variability among 6 individual participants. Right: Dissimilarity of the resting-state network fingerprints (variability in the connectivity fingerprint across participants represented by the Wasserstein distance between unique pairs of participants; **Materials and Methods**) are plotted as a function of each *pmfs* component for left and right hemispheres. Error bars represent 68% CI (SEM) across unique participant pairs.

Figure 6. The *pmfs* and *imfs* components are functionally differentiable based on cognitive components: A meta-analysis of fMRI experimental tasks. (**a**) Schematic of analyses linking sulcal probability maps (bottom, left) and cognitive component maps (right) from a meta-analysis of fMRI experimental tasks (Yeo et al., 2015) using an expectation maximization algorithm (**Materials and Methods**). For each *pmfs* component, the algorithm provides a posterior probability for each of 14 cognitive components being associated with the provided sulcal probability map. (**b**) For each *pmfs* and *imfs* component in each hemisphere, the posterior probability for each cognitive component is plotted. This approach further supports that the *pmfs-p* (Component 12, lh; Component 11, rh), *pmfs-i* (Component 10, lh and rh), and *pmfs-a* (Component 10, lh; Component 9, rh; **Materials and Methods**)

are functionally dissociable based on meta-analytic data of cognitive task activations. The *imfs-h* and *imfs-v* are also dissociable from the *pmfs* components in the left hemisphere, and functionally similar to the *pmfs-a* in the right hemisphere. Gray dots indicate individual participant data points when the analysis is performed with individual labels transformed to a template cortical surface, rather than with probability maps (**Materials and Methods**).

Figure 7. Comparing the overlap between retinotopic responses relative to the predicted location of the *pmfs* sulcal components. Map of the mean (n = 181) R^2 metric (colorbar) from the HCP retinotopy dataset (Benson et al., 2018) on the *fsaverage* template cortical surface for each hemisphere, thresholded at 15%. This metric measures how well the fMRI time-series at each vertex is modeled by population receptive field (pRF) modeling that was calculated and shared by Benson and colleagues (https://osf.io/bw9ec/wiki/home/). Predicted *pmfs* location from the maximum probability maps is overlaid in orange (thresholded at 33% overlap across participants). There was only a modest overlap between predicted *pmfs* location and retinotopic representations (a) in the right hemisphere (no overlap in the left hemisphere). Instead, and consistent with prior work (Mackey et al., 2017), the highest correspondence between retinotopic responses and sulcal patterning in LPFC occurs at two sulcal intersections: 1) the *sprs* and *sfs-p* (c), and (2) the *iprs* and *ifs* (b).

Figure 8. Quantification and prediction of *pmfs-p, pmfs-i, and pmfs-a* within individual hemispheres. (**a**) Procedure to generate sulcal probability maps based on the manual anatomical labeling within each individual participant. Labels from each individual are transformed to a template cortical surface to form a probabilistic sulcal map and then projected onto the surface of a held-out individual participant. The overlap between the manual anatomical label on the held-out participant and predicted location was then calculated for each iteration across participants. (**b**) Overlap (DICE coefficient) between predicted and manual location of each *pmfs* component within individual participants. Prediction for the *pmfs* is highest when all three components are combined. The central sulcus (*cs*) is included as a noise ceiling for reference, as this landmark is used in the surface registration algorithm that aligns cortical surfaces across participants.

Figure 9. Linking the past to the present: Myelination gradients, cortical areas, and the *pmfs*. (**a**) Left: Photograph of a left hemisphere from Sanides (1962). Numbers indicate cortical areas differing in myeloarchitecture. Dotted white lines: Sulcal boundaries as defined by Sanides. Dotted colored lines: *pmfs-p* (green), *pmfs-i* (red), and *pmfs-a* (blue) based on modern definitions used in the present study. Identifying *pmfs* components in Sanides' classic images shows that he identified myeloarchitectonic gradations within *pmfs* components, which is consistent with the present measurements. Gradations occurred in superior-inferior, as well as anterior-posterior dimensions. In the inferior portion of the *pmfs-p* (green), there is an anterior-posterior transition between areas 40 and 55. In the *pmfs-i* (red), there are two transitions: (i) a superior-inferior transition between areas 44 and a transition zone to area 55, and (ii) an anterior-posterior transition between areas 44 and 45. In the *pmfs-a*, there is a transition between areas 45 and 54. Right: Myelination stain of a histological section (coronal orientation) from Sanides (1962). Arrows indicate boundaries between labeled myeloarchitectonic areas (numbers). *pmfs-a* is labeled to help the reader link the myelination stain to the image at left. The reader can appreciate the shallowness of the *pmfs-a* relative to the sulcus (*ifs*) between areas 54 and 58, which is also consistent with our measurements (**Figure 2**). (**b**) Left*:* Maximum probability maps (thresholded at 33% overlap across participants) for the *pmfs-p*, *pmfs-i*, and *pmfs-a* are shown on the FreeSurfer average template (left hemisphere). The probability maps are shown relative to four areas from a multi-modal cortical parcellation based on structural and functional MRI data (Glasser et al., 2016). The *pmfs-a* appears to denote the dorsal to ventral transition between areas 46 and p9/46v in anterior LPFC, while the *pmfs-p* appears to denote the dorsal to ventral transition between areas 8Av and 8C in posterior LPFC. Right: *pmfs* and *imfs* maximum probability maps relative to a resting-state fMRI parcellation with proposed homologous parcels between monkey and human LPFC from Sallet et al., 2013. Here, the *pmfs-i and*

pmfs-a denote the 9/46d and 9/46v boundary, while the *imfs* is situated within area 46. This relationship is also consistent with a recent cytoarchitectonic atlas showing that the *pmfs-a* identifies a transition between 9/46v and 9/46d (Petrides, 2019).

Extended Data Figure Legends

Extended Data Figure 2-1. Individual labeling of the *pmfs* in all participants.
As in Figure 1, the three components of the posterior middle frontal sulcus (*pmfs*) are outlined in white on the individual inflated cortical surface of each participant. For reference, the large superior (*sfs*) and inferior (*ifs*) frontal sulci are also outlined, in blue, along with the horizontal (*imfs-h*) and vertical (*imfs-v*) intermediate frontal sulci, in green.

Extended Data Figure 5-1. Individual resting-state network connectivity profiles for the *pmfs* components. The individual connectivity profiles and *pmfs* sulcal definitions were used to calculate the connectivity fingerprint, which represents the overlap of each network within the *pmfs* component of each participant. Polar plots showing the connectivity fingerprint of the three *pmfs* components (plotted outwards) with each of 17 resting-state functional connectivity networks (Kong et al., 2018) for each individual participant (numbered) for the left hemisphere.

a historical ambiguity regarding the middle frontal sulci (*pmfs*)

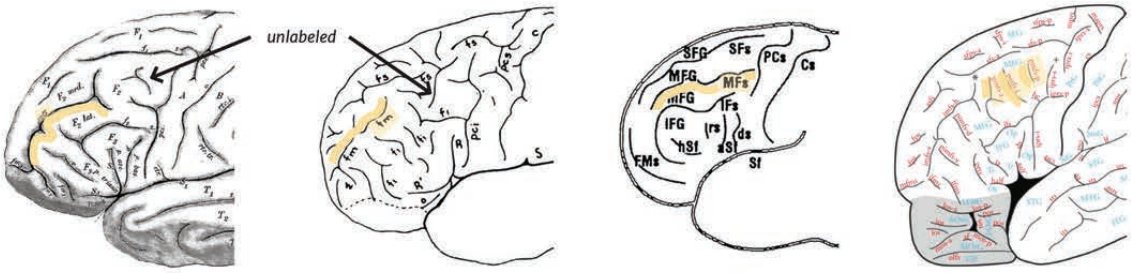

1890 *Eberstaller* | 1950 *Connolly* | 1995 *Rajkowska & Goldman-Rakic* | 2019 *Petrides*

b identification of the middle frontal sulci (*pmfs*) within individuals

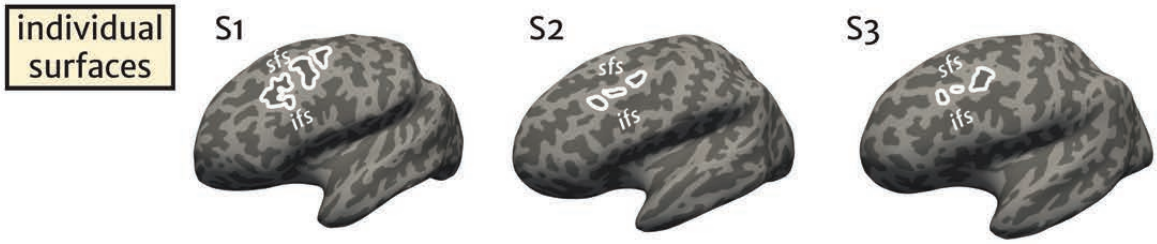

c *pmfs* components are often absent from average cortical surfaces

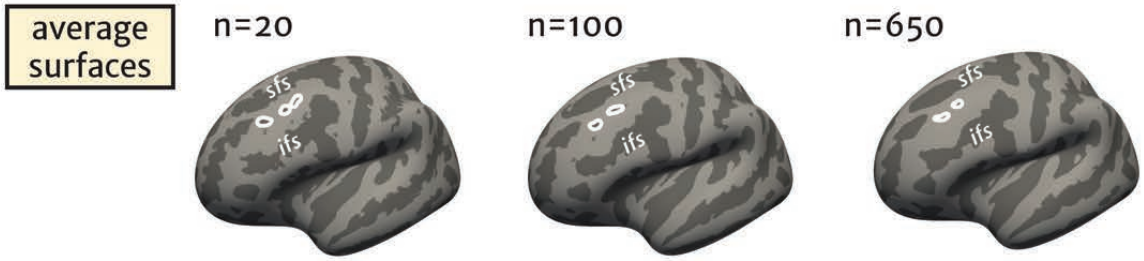

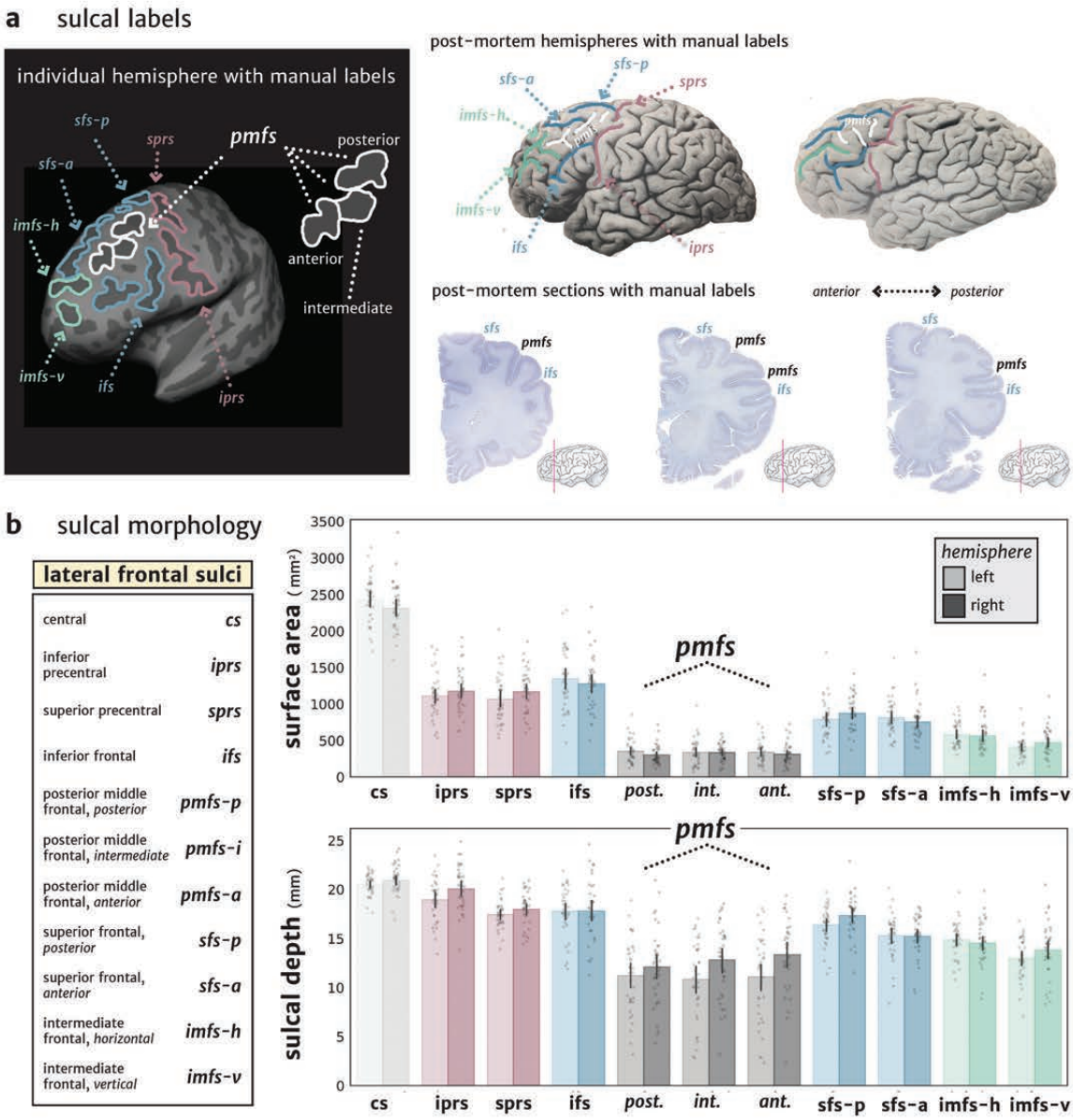

most common intersections	1st	2nd	3rd
pmfs-p	*independent*	*pmfs-i*	*iprs*
lh	44.4%	22.2%	16.7%
	independent	*sfs-a*	*pmfs-i*
rh	30.6%	30.6%	16.7%
pmfs-i	*independent*	*pmfs-p*	*pmfs-a*
lh	47.2%	22.2%	16.7%
	pmfs-a	*independent*	*pmfs-p*
rh	58.3%	27.8%	19.4%
pmfs-a	*independent*	*imfs-h*	*pmfs-i*
lh	47.2%	38.9%	16.7%
	imfs-h	*pmfs-i*	*Independent*
rh	52.8%	50.0%	13.9%

	surface area (mm^2)	depth (mm)
pmfs-a	mean ± s.d.	mean ± s.d.
lh	341.9 ± 154.8	11.1 ± 4.4
rh	315.4 ± 149.7	13.4 ± 3.7
pmfs-i		
lh	339.3 ± 191.7	10.9 ± 4.2
rh	337.8 ± 124.2	12.8 ± 3.8
pmfs-p		
lh	353.6 ± 164.1	11.2 ± 3.8
rh	301.7 ± 133.2	12.1 ± 3.9